

Water exchangeability between pore volumes: a key mechanism governing water diffusion in highly cross-linked polymer coatings

Seyyed Mohammad Mousavifard^a, Mohsen Mohseni^{a,*}, Hossein Yahyaei^a, Hesam Makki^{b,*}

^a Department of Polymer and Color Engineering, Amirkabir University of Technology, 424 Hafez Avenue, Tehran 15875-4413, Iran

^b Department of Chemistry and Materials Innovation Factory, University of Liverpool, Liverpool L69 7ZD, UK

ARTICLE INFO

Keywords:

Acrylic melamine coatings
Water uptake
Water desorption mechanisms
Molecular dynamics
Polymer network

ABSTRACT

Understanding the behavior of water in highly cross-linked coatings, such as melamine-curable systems, is essential for material design, particularly for outdoor applications where water absorption and desorption significantly affect performance. This study demonstrates that the ability of water molecules to navigate interconnected water clusters plays a more crucial role in water diffusion than previously anticipated factors like network polarity or the free volume of the network. Using a multi-scale simulation methodology validated by experimental data, we investigate the interactions and hydrogen bonding between water and various network components, as well as with other water molecules. A detailed analysis of the shapes and distributions of water clusters, along with the pathways of water molecules within the polymer network, reveals a direct relationship between water diffusion and the exchangeability of water between pore volumes. We show that water exchangeability can be tuned through molecular design to control water absorption, trapping, and desorption, all of which impact the material's functionality in applications.

1. Introduction

Complex cross-linked polymer networks are widely used in applications requiring high durability, chemical resistance, and mechanical strength. For instance, melamine-based systems are often employed in automotive coatings due to their long service life and robust performance in harsh outdoor conditions [1–3]. Given the critical role of water in the deterioration of these materials - contributing to blistering, swelling, hydrolysis, and delamination - it is essential to understand how water interacts with these polymer networks [4]. However, the exact relationship between molecular structure and water absorption/desorption is not fully understood. As a result, the molecular design parameters necessary to control water-polymer interactions remain elusive, despite the wide range of monomers and functional groups available for use in such systems [5].

Theoretical models have been developed to explain the behavior of cross-linked polymers upon exposure to the water. These theories are mostly based on the free volume of the network at the glassy or rubbery states of the polymer lacking the incorporation of physical interactions between them [6–10], including different hydrogen bonding and van der Waals interactions with bounded or unbounded water [11,12].

Depending on the chemical structure and variation of the functional groups, polymer networks show considerably different hydrogen bonding behavior, and their interaction with water changes by the degree of the cross-linking, due to the change in the polarity of the system upon cross-linking, affecting the dynamics of water in the matrix. This limits the ability of the existing theoretical models to accurately describe water-polymer interactions, especially in the case of complex polymer networks with various functional groups, network defects, and inhomogeneities [13,14]. Furthermore, due to the multiscale effect of water, from the atomistic-scale interactions (e.g., hydrogen bonding) to macroscopic effects (e.g., blistering and delamination), experimental techniques alone come short in providing a holistic picture, particularly where the atomic forces originate the water-polymer interactions. Molecular dynamics (MD) simulations are shown to be an effective complementary tool at those scales [15–17]. For instance, water diffusion [18–21], water-polymer hydrogen bonding [22–24], formation of water pathways [25–27], water and ion dynamics in nanochannels [28,29], and distribution of water clusters within the network [30,31] can be readily studied through MD simulations, unraveling the molecular origin of the effect of water on polymers.

The predicted behavior of a polymer system in MD simulations is

* Corresponding authors.

E-mail addresses: mmohseni@aut.ac.ir (M. Mohseni), h.makki@liverpool.ac.uk (H. Makki).

directly influenced by its microstructure and atomic orders, indicating the importance of a realistic atomistic model [16,32]. Comprehensive investigations of non-thermoset polymer systems, such as fluoropolymers [33–35] and polyacrylate gels [36–38], provide valuable insights into water-polymer interactions. These studies reveal key aspects such as water permeation pathways in membranes, the clustering behavior of water molecules, their affinity to various functional groups, and the influence of backbone and side-chain structures on water dynamics. However, for thermoset polymers, the investigations have been limited to simplified models [23,39–44] due to the challenges in constructing well-equilibrated and realistic microstructures, especially in high cross-linking conversions where complex prepolymers and high-functional cross-linkers are incorporated [15]. This has led to inconclusive structure-property relationships. For example, it has been shown that cross-linking density in polymer networks affects water uptake through changes in free volume and network polarity [30,44]. However, the ability of water molecules to access these free volumes and form hydrophilic pathways remains unclear. Additionally, while existing studies on polymer-water interactions in low-density cross-linked polyacrylates [23,24] provide valuable insights, they cannot be directly applied to acrylic-melamine coatings due to the distinct water pathways in the highly cross-linked matrices.

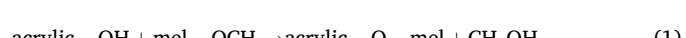
This study aims to provide insights into the atomistic-level interactions between water and a rather complex acrylic-melamine system through combined simulation and experimental investigations. Using a multi-scale simulation approach, we first employed a dynamic real-time polymerization scheme in coarse-grained (CG) MD simulations [45], ensuring a well-equilibrated initial configuration for highly cross-linked thermoset polymers. We then used a reverse-mapping procedure to capture atomistic interactions between the polymer and water, addressing challenges associated with modeling hydrated, complex networks. Our study uncovers key water diffusion mechanisms, identifies interaction sites, explores the persistence of water molecules, and examines trapping effects leading to polymer degradation and delamination. These findings are crucial for guiding the design of more robust materials, particularly those with enhanced hydrolytic durability and improved resistance to moisture-related degradation.

2. Method

2.1. Materials and sample preparation

An acrylic resin containing the same molar ratios of styrene, methyl methacrylate (MMA), 2-hydroxyethyl acrylate (HEA), butyl acrylate (BA), and 2 wt% acrylic acid monomers with M_n of 5818 g/mol was synthesized in solution polymerization and methoxy propyl acetate (MPA) as the solvent. A more detailed characterization of the synthesized resin is presented in SI section 1.1. CYMEL 303 (supplied from Allnex), which is a highly methylated monomeric melamine, containing 98 % hexa(methoxymethyl)melamine (HMMM) with M_w of 354 g/mol was used as the cross-linking agent. A blend of MPA (20 %) and xylene (80 %) was prepared as solvent for adjusting the viscosity of the resin mixture during application. All monomers and solvents were purchased from Sigma-Aldrich with purity >99 %.

The curing of acrylic resins with melamine cross-linkers occurs at elevated temperatures resulting in a highly cross-linked thermoset network according to the following main reaction:



Mixtures with molar ratios of 1:1.2 and 1:1.5 of acrylic to melamine functional groups (corresponding to 20 % and 50 % excess melamine compared with stoichiometric ratio) were prepared. The required solvent for achieving 60 % wt. solid content was added to the mixture and stirred for 30 min. Then, 1 g of the resin mixture was cast on a silicon mold and cured in a convection oven at 150 °C for different times (see Table 1). The free films with thickness of 400 ± 20 μm were used for gravimetric and ATR-FTIR measurements.

2.2. Characterization

2.2.1. ATR-FTIR

ATR-FTIR spectroscopy of uncured resin mixtures and free film samples cured for different times was performed using a Bruker FTIR spectrometer (Germany) equipped with an ATR accessory. The spectra were acquired in the range of 4000–400 cm⁻¹ with a resolution of 1 cm⁻¹.

2.2.2. Gravimetric measurements

Free-standing films with 3 cm diameter were immersed in deionized water at 27 °C and 85 °C. The samples were removed from the water at the specified time intervals and weighed with a precision of 0.1 mg. Before weighting, the excess water on the surface of the samples was wiped with a dust-free cotton paper. For ensuring repeatability, 9 replicas were used for the measurements and the averaged value and standard deviation are reported in the final results. For desorption measurements, the same samples were placed in a convection oven held at 27 °C.

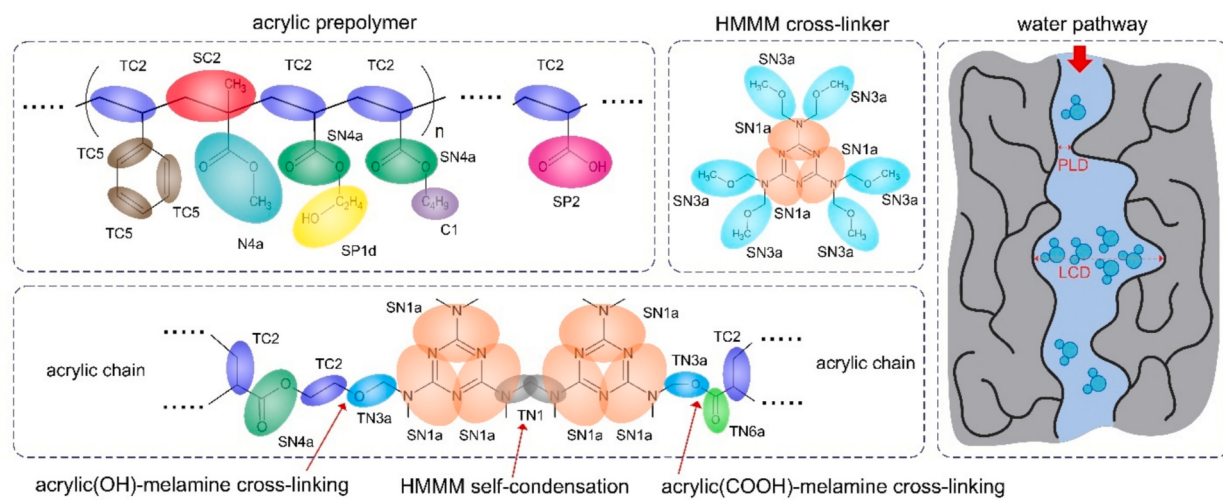
2.3. Simulation procedures

The initial atomistic structures of acrylic resin and HMMM cross-linker were constructed and optimized using Density Functional Theory (DFT) calculations employing B3LYP/6-31G* and partial charges were calculated using ESP method by using Gaussian 16. All-atom simulations were carried out using OPLS-AA force field [46] for bonded and nonbonded interactions and employing TIP4P model for water [47]. LINCS algorithm was applied to constrain the hydrogen bonds in the system [48]. All MD simulations were carried out using GROMACS 2022 [49].

CG scale simulations enable us to achieve a highly cross-linked structure, which is not achievable by only using all-atom simulations, due to their slower relaxation dynamics leading to limited accessible timescales. Utilizing CG scale facilitates the construction of high conversion degree networks by enabling faster chain mobility and smoother potential landscape, thereby overcoming the challenges of kinetic trapping and excessive molecular friction encountered at the AA level. Accordingly, the thermoset networks were constructed in CG scale employing Martini 3force field [50] (see details of CG parameterization and force field validation in SI section S2.1, S2.2). The atomistic and the relevant CG structures of network constituents are depicted in Scheme 1 (top panels). For both H2O and H50 formulations, the required number of melamine and acrylic chains were randomly inserted in the simulation box, resulting in boxes of approximately 10,000 beads. Following energy minimization and box packing, the system was relaxed for 150 ns

Table 1
Different samples prepared for experimental analyses.

Acrylic/melamine molar ratio (label)	1/1.2 (H2O)				1/1.5 (H50)			
Curing time (min)	5	10	20	40	5	10	20	40
System name	H2O-5m	H2O-10m	H2O-20m	H2O-40m	H50-5m	H50-10m	H50-20m	H50-40m



Scheme 1. Atomistic and coarse-grained structures for acrylic and melamine before (top) and after (bottom) the reactions based on Martini 3 bead typing. Each bead type is represented in a distinct color. Schematic of LCD and PLD in a network containing water (right).

under NPT conditions employing a time step of 10 fs at 300 K and 1 bar controlled by V-rescale and C-rescale methods, respectively [51,52].

The cross-linking simulation was performed using PolySMart package [45]. The cut-off radius for the reaction was set to $\pm 5\%$ of the Lennard Jones radii of the reacting beads. The reaction probabilities for COOH and OH containing beads with the melamine reacting beads were set to be equal, and the self-condensation of HMMM was set to 2 % of the acrylic-melamine main reaction according to Ref [53]. The cross-linking procedure contains iterative reaction cycles at which the last frame is extracted, and the reaction occurs based on the defined parameters and followed by updating the topological information of the beads in the system. Each reaction cycle contains an energy minimization followed by a 50 ps relaxation with 1 fs time step, and then 1 ns relaxation with 5 fs time step. The constructed CG structures after the reaction are depicted in Scheme 1 (bottom panel). The cross-linking reactions were performed on five independent initial configurations and all reported properties are the averages of these samples.

Although, CG scale simulations allow the structure to be relaxed at large scales, exploring the fine-scale details, such as hydrogen bonding and solvent interactions requires an all-atom structure and further relaxations at atomic-level to ensure a stable structure. Therefore, to investigate the atomicistic thermoset network, which is essential for the calculation of water interactions, the networks were reverse mapped to all-atom scale using the backward procedure of Martini [54], detailed in SI section S2.3. The hydrated networks were constructed by randomly inserting a predetermined number of water molecules in the atomistic network model. Then, the hydrated models, simulation boxes containing about 55,000–60,000 atoms, were relaxed for 30 ns under NPT condition ($T = 300\text{ K}$, $P = 1\text{ bar}$) with a time step of 2 fs and utilizing V-rescale thermostat and C-rescale barostat.

The diffusion coefficient of water is directly related to the extent of the water molecule's mobility in the media. In MD simulations the mean square displacement (MSD) of water can be calculated during the simulation period, providing the diffusion coefficient according to Eq. 2:

$$D = \lim_{t \rightarrow \infty} \frac{d}{dt} \text{MSD} = \lim_{t \rightarrow \infty} \frac{d}{dt} \left(\frac{1}{6N} \sum_{i=1}^N (\vec{r}_i(t) - \vec{r}_i(t_0))^2 \right) \quad (2)$$

where N is the number of water molecules and r represents the center of mass position of the water molecule. Accordingly, D can be estimated from the slope of the MSD curve in the linear region.

The pore structure of dry and hydrated networks was analyzed utilizing Poreblazer 4.0 [55], employing Helium and water probes as a representation of total free volume and water accessible free volume in

the network, respectively. Pore limiting diameter (PLD) and largest cavity diameter (LCD) parameters were calculated to characterize the structure of pore volumes. As depicted in Scheme 1 (right panel), the LCD characterizes the largest pore volumes prone for water molecules aggregates within and the PLD controls the selectivity level of channels for penetrant molecule exchange between the pores.

To simulate the desorption mechanism of water from the coating, a constant force of 50 KJ/mol/nm is applied to a single water during 20 ns in the simulation box in x direction and the trajectory is analyzed. To capture the behavior of all water molecules, this process is performed on 20 different random water molecules in the box. Subsequently, the travel distance and the nearby atoms (in a specific cutoff distance) for the water molecule during the simulation were investigated.

3. Results

3.1. Network polarity

Fig. 1a presents the ATR-FTIR spectra of H50 samples at various curing times, confirming the presence of aromatic ($\sim 1450\text{--}1600\text{ cm}^{-1}$), aliphatic ($\sim 1100\text{, }2900\text{ cm}^{-1}$), hydroxyl ($\sim 3500\text{ cm}^{-1}$), and ester ($\sim 1730\text{ cm}^{-1}$), groups in the structure. The suppression of the O–H stretch absorption band (around $3200\text{--}3600\text{ cm}^{-1}$) upon curing confirms the consumption of hydroxyl groups during the reaction. This suppression, normalized against the strong C=O stretch absorption band (around 1730 cm^{-1}), which remains unaffected during the reaction, is used to calculate reaction conversions. Additionally, the decrease in the intensity and area of C–H stretch absorption band (around 2900 cm^{-1}) indicates the consumption of methoxy groups in melamine, accompanied by the evaporation of methanol during the cross-linking process, providing further evidence of the curing reaction. As summarized in Table 2, conversion values obtained using both peak areas are comparable. Minor differences may arise from melamine self-condensation, which affects the C–H absorption.

ATR-FTIR spectroscopy was also performed on H20 samples (detailed in SI Section S1.2), revealing lower conversions at equivalent reaction times compared to H50 samples.

Consistent with the ATR-FTIR results, the normalized number of unreacted hydroxyl and carboxyl groups in the acrylic chains, along with the calculated conversion as a function of simulation time (Fig. 1b) demonstrates a rapid reaction rate during the initial stages, followed by a slower progression toward completion—characteristic of polycondensation reaction kinetics [56]. As expected, the trends for the consumption of OH and COOH groups are generally similar, with the

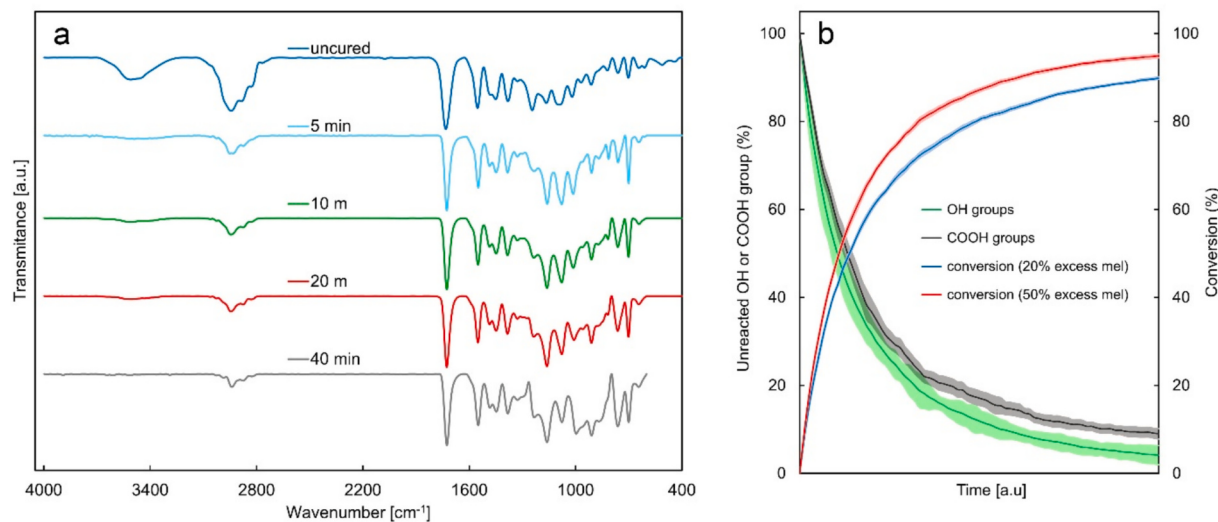


Fig. 1. a) ATR-FTIR spectra for uncured and cured samples of H50. b) The trend of conversion and unreacted groups of acrylic chain over time obtained from simulations (the shadowed region represents the standard deviation).

Table 2

The calculated conversions for H50 samples at various reaction times.

Curing time (min)	Conversion based on OH peak	Conversion based on CH peak
5	67.4 %	61.9 %
10	74.9 %	68.7 %
20	82.4 %	75.5 %
40	89.9 %	82.3 %

slightly lower consumption rate of COOH likely attributed to its lower initial concentration. Furthermore, as observed experimentally, Fig. 1b reveals higher conversion values for H50, owing to the greater availability of cross-linkers and a higher extent of reactions. These agreements between experimental and simulation results validate the accuracy of the reaction simulation.

3.2. Free volume analysis

Pore analysis of the equilibrated atomistic structure of the thermoset matrices is crucial for identifying potential water penetration sites. The pore size distribution of the networks at various curing times for H20 and H50 samples (Table S11) reveals no significant changes in the overall pore structure. However, isolating the pores accessible to water molecules (detailed in SI, section S3.1) from the rest reveals distinct trends.

Fig. 2 illustrates the theoretical water-accessible free volume of the networks during the curing process. As shown, curing increases the water-accessible free volume for both H20 and H50 systems. Similar behavior has been reported for other thermoset systems [44] and can be attributed to the trapping of unoccupied free volumes within the structure at higher conversion levels. This phenomenon arises due to the increased formation of new bonds and the immobilization of network components, which restrict chain mobility and prevent the occupation of free volumes by the network itself. While the percentage of water-accessible free volume at each curing time does not differ significantly with varying melamine content, slightly lower values are observed for higher melamine content. This difference can be attributed to the more efficient packing of smaller melamine components compared to the longer chains of acrylic polymers.

3.3. Water interactions

The water uptake of H50-5m and H50-20m samples was measured

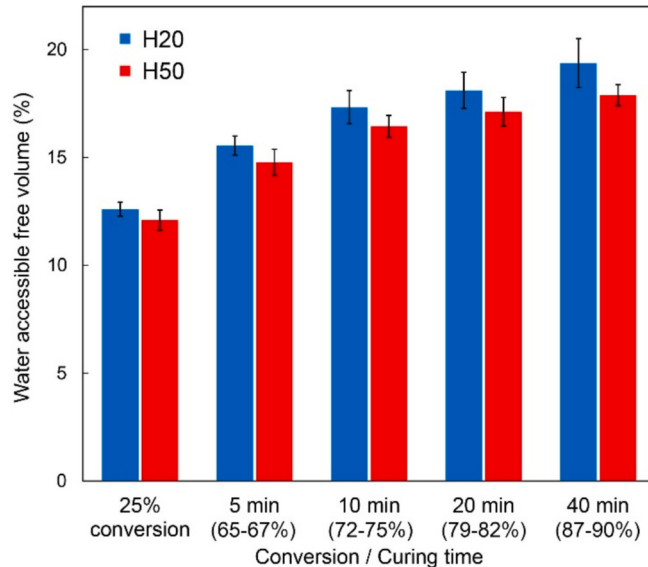


Fig. 2. The water-accessible free volume of the networks of the samples cured for various curing times. Since the minimum curing time for producing a tack-free coating film in the laboratory is 5 min, which is equivalent to 65–67 % conversion, for very low conversion of 25 % no equivalent curing time is mentioned.

using gravimetric experiments. Fig. S9a shows water uptake as a function of immersion time. Depending on the curing time, water uptake ranged between 2 and 8 wt%. In comparison, hydrated models of H50, containing 2.5–15 wt% water, were made by randomly inserting water molecules into the simulation box and relaxing the hydrated model for approximately 30 ns under NPT conditions (300 K and 1 bar). The representation of the water distribution within the different hydrated networks are shown in Fig. S7.

Fig. 3a presents the radial distribution function (RDF) and coordination number between water molecules and various oxygen atoms in the polymer network for the H50-20m sample with 2.5 wt% hydration. The analyzed groups include: (i) carbonyl groups (in MMA, HEA, and BA), (ii) hydroxyl groups (from unreacted OH in the HEA units), (iii) methoxy groups (in unreacted melamine cross-linkers), (iv) alkoxy groups (in reacted melamine with acrylic chains), and (v) ester groups

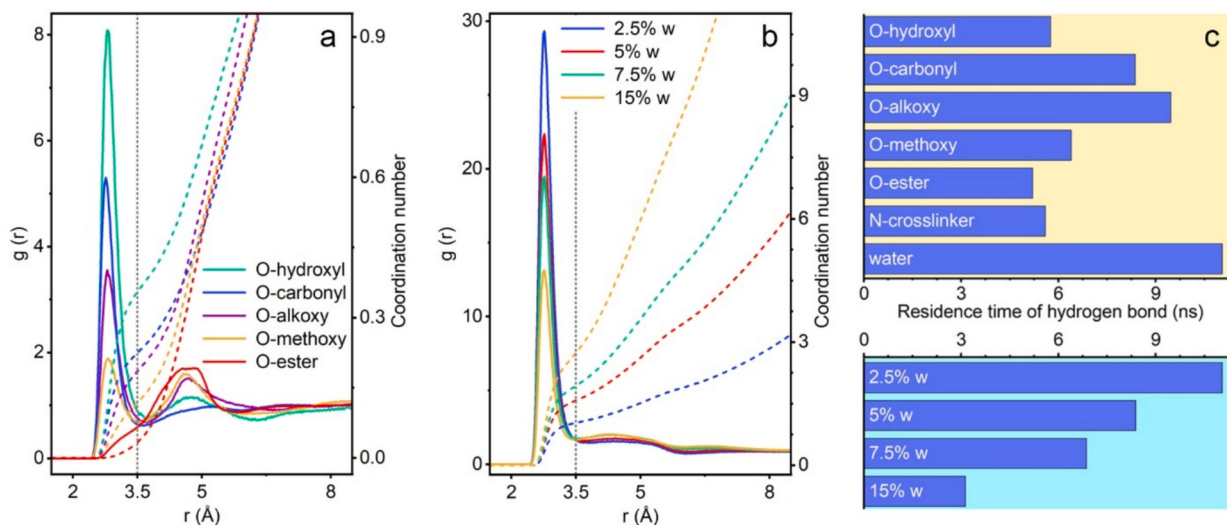


Fig. 3. RDF (solid lines) and coordination number (dashed lines) plots in H50-20m sample, for a) oxygen atom of water (at 2.5 wt% hydration level) with various oxygen atoms of the network, b) oxygen atom of water molecules with each other at different hydration levels. c) Residence time for hydrogen bonding of water in H50-20m sample with various polar atoms of the network at 2.5 wt% hydration level (top panel) and with other water molecules at different water levels (bottom panel).

(in MMA, HEA, and BA units).

All RDFs, except for the ester group, exhibit a prominent peak at ~ 2.8 Å, indicating strong hydrogen bonding between water molecules and these polar groups within their first hydration shell. The second hydration shell appears as a peak at $4\text{--}5$ Å. Within the hydrogen bonding range (< 3.5 Å) [57–59], the coordination number reveals a significantly higher density of water molecules around the hydroxyl groups compared to other polar groups. This observation suggests that the removal of hydroxyl groups during cross-linking reduces the overall polarity and water affinity of the network, despite the slightly higher affinity of water for alkoxy groups (at cross-linking points) compared to methoxy groups (unreacted melamine). Additionally, the low coordination number for ester oxygen atoms confirms the absence of strong hydrogen bonding with water. This behavior can be attributed to the greater polarity and lower steric hindrance of nearby carbonyl oxygen atoms, which preferentially attract water molecules.

The RDF shown in Fig. 3b illustrates the water-water interactions for the H50-20 m system with varying hydration levels. In all cases, the presence of hydrogen bonds between water molecules is evidenced by the appearance of a peak at ~ 2.8 Å. At a distance of ~ 3.5 Å, corresponding to hydrogen bonds between neighboring water molecules, the coordination number of water is found to be 1, 1.5, 2, and 2.7 for water contents of 2.5, 5, 7.5, and 15 wt%, respectively. This indicates an increase in the average number of water-water hydrogen bonds with increasing water content, likely due to the formation of larger aggregates of water molecules.

The RDF plot between water and nitrogen atoms on the melamine cross-linker (Fig. S6) indicates minimal hydrogen bonding capability between these groups and water. The results suggest a lower affinity of nitrogen atoms for water compared to oxygen atoms, likely due to steric hindrance effects that make it more difficult for water molecules to pack near the nitrogen sites.

Hydrogen bonding between water and the various polar species within the network is a dynamic process, characterized by frequent formation and breakage as water molecules navigate through the network structure. Using the method explained in SI section S2.4, we calculated the average residence time of water molecules near different polar groups in the polymer network (Fig. 3c).

Fig. 3c (top panel) reveals the shortest residence time for ester oxygen and cross-linker nitrogen pairs, indicating weak interactions and a limited capacity for hydrogen bonding. Additionally, the hydrogen bond

lifetime between water and hydroxyl groups is observed to be lower than that for carbonyl and alkoxy oxygen atoms, despite the hydroxyl oxygen's higher polarity and the greater number of water molecules absorbed into this group compared to the carbonyl and alkoxy oxygens. This discrepancy underscores the role of chain mobility in influencing the lifetime of hydrogen bonds with water. The hydroxyl group, located at the end of the acrylic polymer's flexible side chain, exhibits greater freedom of movement compared to the carbonyl and alkoxy oxygens, which are restricted within the polymer backbone. As a result, the increased mobility of the hydroxyl group leads to more frequent formation and dissociation of hydrogen bonds. This dynamic behavior, coupled with the higher availability of water molecules in the vicinity, facilitates the continuous switching of hydrogen bonds between the hydroxyl groups and surrounding water molecules.

Furthermore, the residence time of hydrogen bonds between water molecules for the H50-20m sample, shown in Fig. 3c (bottom panel), is inversely related to the hydration level. This indicates that greater water availability within the aggregates leads to more frequent exchanges of hydrogen bonds between different water molecules.

3.4. Water diffusion

Fig. S5 presents the MSD curves of water molecules in H50 samples containing 2.5 wt% water, along with the calculated diffusion coefficient (D) derived from the MSD curves using the method outlined in method section, as plotted in Fig. 4a. The diffusion coefficient decreases from approximately 1.1×10^{-7} cm 2 /s at 25 % conversion to 0.75×10^{-7} cm 2 /s at 90 % conversion, indicating a statistically significant downward trend based on the standard deviation. The results reveal that extended curing of the networks restricts the movement of water molecules due to the formation of a more densely cross-linked network, leading to a decrease in the water diffusion coefficient. However, even at 25 % conversion, which corresponds to a pre-gel state prior to network percolation and physical film formation, the observed diffusion coefficient remains significantly lower, by nearly two orders of magnitude, than that of bulk water ($\sim 2.3 \times 10^{-5}$ cm 2 /s at 298 K), reflecting the hydrophobic nature of the polymer restricting formation of large water clusters.

As discussed in the previous section, the number of polar groups and the overall hydrophilicity of the system decrease with increased curing time. At the same water content, higher polarity structures typically

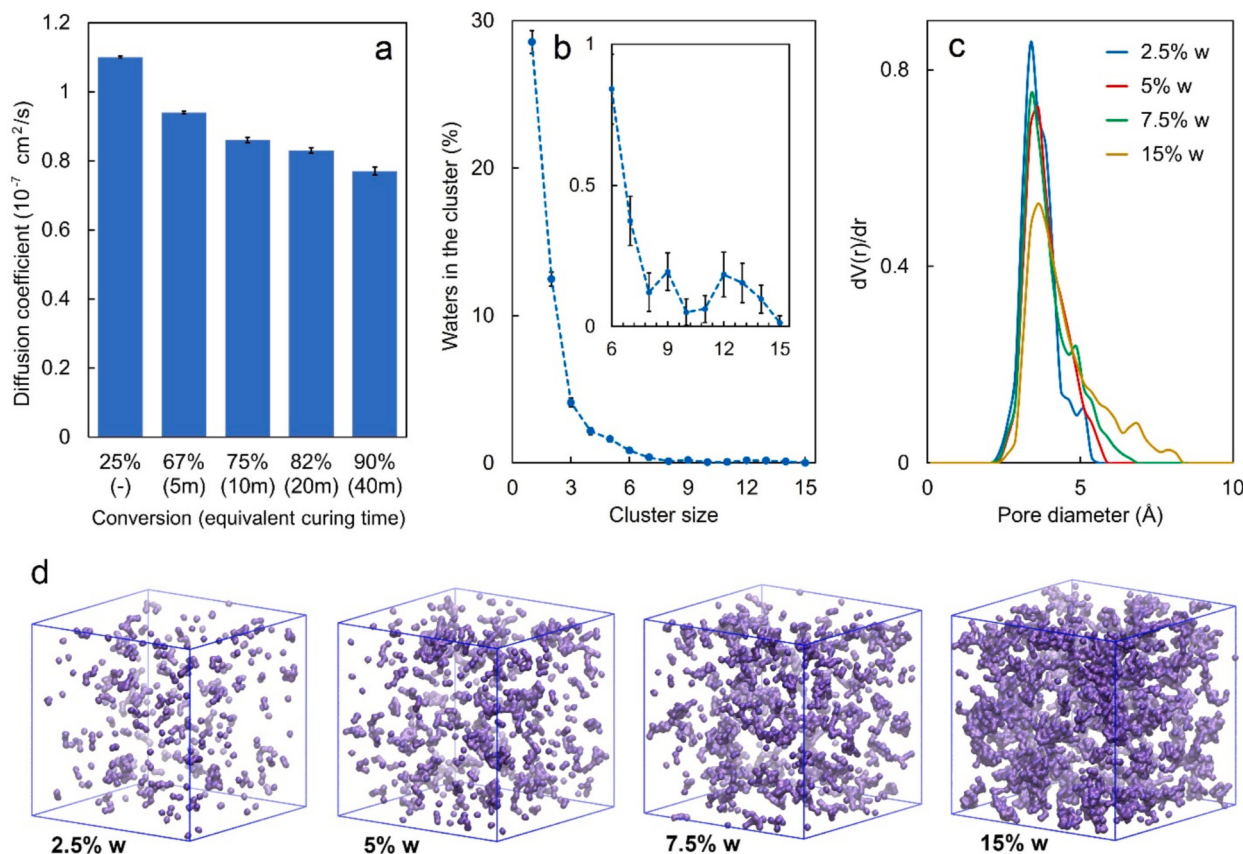


Fig. 4. a) Calculated diffusion coefficient of water in H50 network at different conversions containing 2.5 wt% water. b) The amount of water molecules present in different cluster sizes for H50-20m network. c) The pore size distribution of H50-20m network with different water levels after removing water molecules from the structure file. d) The distribution of water within the H50-20 m hydrated network after a 30 ns relaxation.

reduce water mobility by forming more hydrogen bonds between water and the hydrophilic groups in the network. This increase in hydrogen bonding was also corroborated by the RDF results discussed earlier.

Conversely, it was shown that the total water-accessible free volume of the network increases with curing time, providing more space for water molecules to move within the structure. These opposing factors—reduced polarity and increased free volume—do not align with the observed decreasing trend in the water diffusion coefficient as curing time increases. This suggests the presence of another factor that dominates the effects of polarity and free volume, influencing the vulnerability of the coating to moisture diffusion and water mobility within the network.

Using the method described in SI section S2.5, the size of water clusters was calculated for the H50-20 m system at various water contents considering the cutoff value obtained from Fig. 3b and stated in other literature [59]. Any water molecule within 0.35 nm of a cluster's water molecule is considered part of that cluster. Fig. 4b illustrates the distribution of clusters for 2.5 wt% water, showing a very low population of clusters containing more than three water molecules (see Fig. S3 for other systems). Table 3 summarizes the average percentage of water

present as single molecules and the proportion of water in the largest cluster formed within the simulation box. As water content increases, the percentage of single water molecules decreases significantly—from over 28 % at 2.5 wt% hydration to approximately 2.5 % at 15 wt% water content. Additionally, the size of the largest cluster in the network grows with increasing water content. At 15 wt% water, around 27 % of water molecules aggregate into a single large cluster, whereas the largest clusters in systems with 2.5, 5, and 7.5 wt% water account for only 2.65 %, 2.69 %, and 3.71 % of the total water molecules, respectively.

These observations suggest that, at lower water contents, the increase in water content primarily leads to a higher number of small water clusters without a significant change in their size. However, at sufficiently high water contents, a sudden increase in cluster size occurs as smaller water aggregates coalesce into larger clusters.

To further investigate the shape of water clusters, after equilibration of hydrated models, we removed the water molecules from the simulation box and analyzed the resulting pore structures for the H50-20m sample previously hydrated with 2.5, 5, 7.5, and 15 wt% water contents. As shown in Fig. 4c, the pore size distribution remains relatively unchanged up to 7.5 wt% water content. However, at 15 wt% water, the distribution shifts toward larger pore sizes, accompanied by a decrease in the number of smaller pores. The visualization of water molecules within the networks at various hydration levels, represented in Fig. 4d, also reveals dispersed water aggregates up to 7.5 wt%, followed by the formation of percolating clusters at 15 wt%. This result aligns with the observed clustering behavior of water within the network, indicating that the smaller pore volumes merge into larger ones as more water enters the system. The ingress of water facilitates the formation of connections between adjacent pores, leading to the emergence of larger pore structures.

Table 3
Water cluster analysis results for H50-20m network in different water levels.

Water content (% wt.)	Single water molecules (%)	Largest cluster size (no. of waters)	Waters in the largest cluster (%)
2.5	28.6 (± 0.77)	13.4 (± 0.78)	2.65 (± 0.15)
5	12.6 (± 0.36)	27.1 (± 3.7)	2.69 (± 0.37)
7.5	9.0 (± 0.23)	56.3 (± 5.5)	3.71 (± 0.39)
15	2.5 (± 0.12)	818 (± 144)	27.0 (± 4.77)

A more precise investigation of free volumes of the network was performed by calculating pore limiting diameter (PLD) and largest cavity diameter (LCD) values in structures after removing water molecules. Figs. 5 a and b illustrate the changes in LCD and PLD for H50 system at various curing times and water contents. LCD values show a continuous upward trend with increasing water content, regardless of network conversion, suggesting that water aggregates enlarge existing pores. In contrast, the PLD exhibits a less consistent trend, with minor changes in lower water contents across all conversions. This discrepancy between LCD and PLD indicates that increasing water content promotes the formation of larger water clusters within pores without creating pathways between them, highlighting the structural heterogeneity in the network as has been previously reported for similar systems [60,61]. Notably, at approximately 15 wt% water, PLD increases sharply to 0.24–0.28 nm, aligning with the size of a water molecule ($\sim 2.65 \text{ \AA}$). This abrupt rise reflects the overcoming of structural constraints, allowing water molecules to widen channels between previously isolated pores. Consequently, at higher water contents, the network swells, enabling potential pathways between water clusters. Additionally, the almost constant LCD and PLD values for dry networks across different conversions suggest that cross-linking does not significantly alter pore structures. However, networks with lower conversion exhibit slightly larger PLD values at all hydration levels. This behavior highlights how reduced cross-link density allows greater segmental motion (by swelling due to water ingestion), facilitating channel formation, whereas higher conversion networks restrict such movement due to tighter bonding and limited chain mobility, despite the same pore structures in dry conditions.

The diffusion coefficient of water in networks with varying water contents is shown in Fig. 5c, with corresponding MSD curves in Fig. S5. At lower water contents (up to 2.5 wt%), the diffusion coefficient remains nearly constant across all network conversions. However, as water content increases, a slight rise in the diffusion coefficient is observed, followed by a sharp increase at 15 wt% water. This trend parallels the PLD increase with water content, supporting the earlier observations on PLD and clustering behavior. This correlation aligns with the observations for small penetrant mobility in uncross-linked polymer membranes, highlighting the same diffusion mechanisms validated experimentally [62] and observations in hydrogels [63]. At lower PLD values, water mobility is restricted as the exchange between clusters is limited. The addition of more water overcomes this restriction as the PLD approaches the size of the water molecule ($\sim 2.65 \text{ \AA}$), enabling the formation of pathways between clusters. This structural change

significantly enhances molecular mobility, reflected in the increased diffusion coefficient. The higher slope of the diffusion coefficient increment by the water level in the lower conversion networks, re-confirms the easier capability of water molecules for navigating in matrices with lower structural constraints. These findings underscore the critical influence of microstructural configurations on water mobility within the complex acrylic-melamine networks.

The desorption process of water from a coating originates from the concentration gradient between the network and the surrounding environment, causing the water molecules to migrate to the surface and evaporate. This process can be approximated by applying a force to a water molecule and analyzing its trajectory within the network.

Fig. 6a illustrates the displacement of a pulled water molecule over a 20 ns simulation in the H50-20m sample, averaged over 20 different water molecules in the simulation box. As expected, the average travel distance of water increases with hydration level, aligning with the diffusion coefficients obtained from equilibrium MD simulations. The high standard deviation of the curves reflects significant variability in individual water molecule behavior, likely due to differences in their local environment.

To further investigate this behavior, the number of nearby water molecules (within 0.35 nm, considered part of the same cluster) was calculated and plotted alongside the travel distance for two water molecules in Fig. 6b and c. The visual illustration of the travel route for the pulled water is presented in Fig. S7. As the pulled water molecule moves across the simulation box, it occasionally remains in nearly constant positions for certain periods (comparable to the hydrogen bond residence times in Fig. 3c), indicating a hopping mechanism. A detailed analysis of these hopping points reveals an instantaneous increase in the number of nearby water molecules.

This phenomenon, observed at both high and low hydration levels, suggests that at each plateau region of the position curve, the water molecule is transiently adsorbed at specific network sites, primarily via hydrogen bonding with polar species, which restricts its mobility. Desorption from these sites is facilitated by the approach of additional water molecules, enabling hydrogen bond rearrangement and allowing the molecule to hop to an adjacent absorption site.

While additional factors related to the coating or environment may influence desorption, from the perspective of water movement, the presence and proximity of water molecules and clusters enhance the desorption capability of the network. As desorption progresses, the continuity and population of these aggregates decrease, leading to a lower desorption rate in the final stages. This reduction may result in

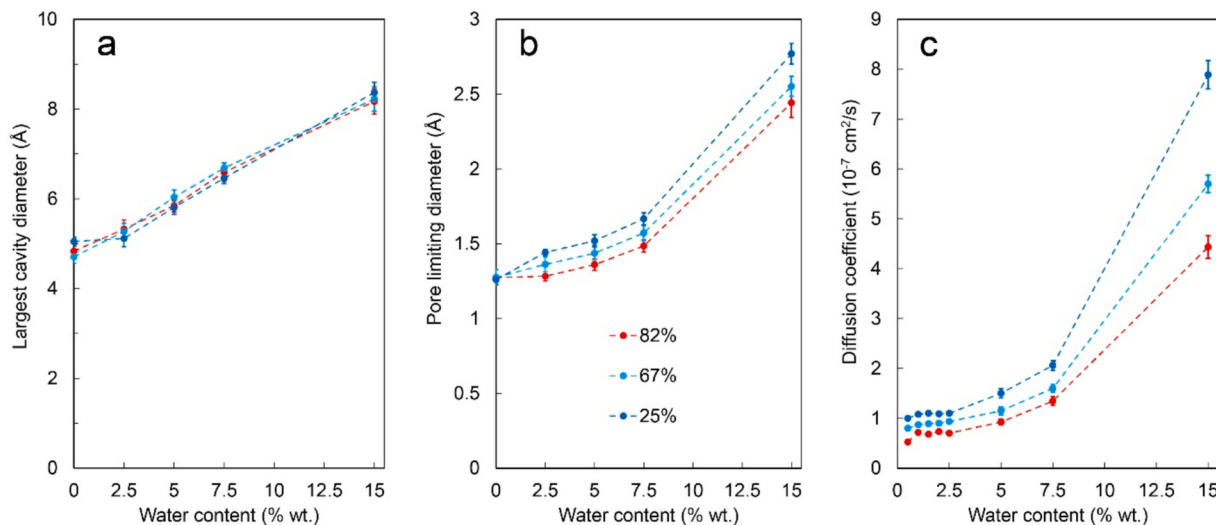


Fig. 5. The trend of LCD (a) and PLD (b) values calculated after removing water molecules and the diffusion coefficient of water (c) for different conversions of H50 network with different water levels.

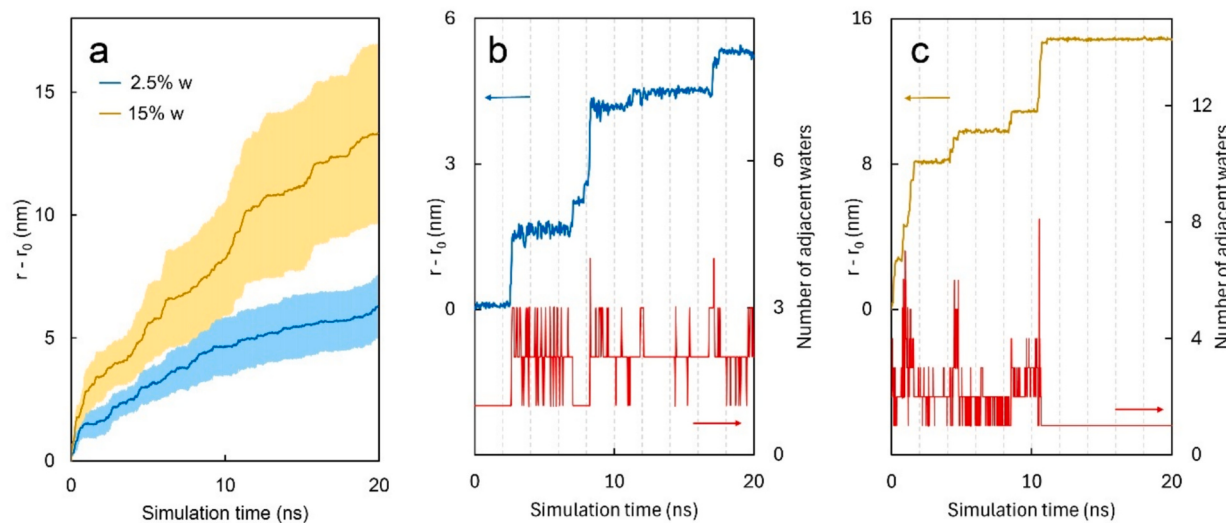


Fig. 6. a) The average displacement of a pulled water molecule during the simulation trajectory in H50-20m sample. An example of change in the position of an individual water molecule and the fluctuations in the number of adjacent water molecules for a water molecule pulled in b) 2.5 wt% and c) 15 wt% hydrated network of H50-20m.

water trapping at absorption sites, particularly in highly polar networks or when a strong driving force for water mobility is absent.

The desorption trends of the cured samples, measured gravimetrically, are plotted in Fig. S9b and summarized in Table 4. As observed, the more polar network (H50-5m) absorbed a greater amount of water, with some residual water remaining in the coating even after 5 h of desorption at ambient temperature. This finding supports the desorption mechanism proposed by MD simulations. Furthermore, comparing the retained water in the same sample (H50-20m, representing a properly cured coating) after immersion at different temperatures underscores the critical role of the driving force (or activation energy) required for complete water release. Higher-temperature water exposure leads to increased absorption, suggesting a discrepancy between theoretical and effective water-accessible free volume. Consequently, full desorption at ambient temperature becomes unattainable.

Therefore, in highly cross-linked systems, the accessibility of free volume to penetrant molecules and their ability to navigate between clusters are critical factors. Consequently, the geometrical constraints of the structure often play a more significant role than free volume itself. This challenge becomes even more pronounced in highly cross-linked and compositionally diverse networks, such as acrylic-melamines, where functionalized cross-linkers and varying polarity further complicate desorption behavior.

4. Conclusions

This study emphasizes the complexity of water diffusion in highly cross-linked polymers (e.g. acrylic-melamine), revealing critical factors that have often been overlooked. Our study shows a decline in water diffusion with increased reaction conversion, despite reduced polar groups and increased pore volumes during curing. This suggests that an additional factor, likely related to pore network connectivity, overrides the effects of polarity and free volume. The findings highlight the significant role of water molecule exchangeability in polymer-water interactions, which proves to be more influential than previously recognized. The hydrogen bonding behavior between penetrant water molecules, network components, and other water molecules underscores the importance of monomer selection in synthesis for developing more durable, water-resistant materials.

Analysis of the diffusion coefficient trend in conjunction with pore-limiting diameters (PLD) in highly cross-linked materials further supports the idea that water diffusion is mainly driven by pore

Table 4
Water uptake and desorption results of gravimetric measurements.

Sample/uptake temp.	Equilibrium water uptake (%)	Equilibrium residual water in the coating after desorption (%)
H50-5m / 25 °C	7.7 (± 0.14)	0.09 (± 0.01)
H50-20m / 25 °C	2.1 (± 0.05)	0
H50-20m / 85 °C	2.5 (± 0.05)	0.25 (± 0.02)

interconnectivity and structural constraints, especially at high conversions—unlike in networks formed by low-functional cross-linkers such as epoxies [59]. These constraints can affect the free volumes of the network, causing a discrepancy between theoretical and effective water-accessible free volume.

Water desorption from the network is restricted by (i) the presence of polar groups that form hydrogen bonds with water, and (ii) by discontinuity of water clusters. While desorption occurs more easily in connected pore networks, densely cross-linked structures can trap and isolate water clusters, increasing susceptibility to hydrolytic degradation over time. On the other hand, low conversion networks, often contain more polar groups and can retain water through stronger hydrogen bonds near polar sites, requiring elevated temperatures to release all absorbed water. Thus, the combination of the presence of highly polar groups and geometric confinement effects makes coating weaker to water and moisture contamination.

CRediT authorship contribution statement

Seyyed Mohammad Mousavifard: Writing – original draft, Validation, Methodology, Investigation, Formal analysis. **Mohsen Mohseni:** Writing – review & editing, Investigation, Conceptualization. **Hossein Yahyaei:** Investigation. **Hesam Makki:** Writing – review & editing, Supervision, Methodology, Conceptualization.

Declaration of competing interest

The authors declare that they have no known competing financial interests or personal relationships that could have appeared to influence the work reported in this paper.

Acknowledgements

This work made use of the facilities of the N8 Centre of Excellence in Computationally Intensive Research (N8 CIR) provided and funded by the N8 research partnership and EPSRC (Grant No. EP/T022167/1). The Centre is coordinated by the Universities of Durham, Manchester, and York.

Appendix A. Supplementary data

Supplementary data to this article can be found online at <https://doi.org/10.1016/j.porgcoat.2025.109405>.

Data availability

Data will be made available on request.

References

- [1] H. Song, J. Xiao, Y. Huang, Multiscale modeling and optimization of Nanoclearcoat curing for energy efficient and quality assured coating manufacturing, *Ind. Eng. Chem. Res.* 55 (2016) 3351–3359, <https://doi.org/10.1021/acs.iecr.5b03167>.
- [2] R. Tian, K. Li, Y. Lin, C. Lu, X. Duan, Characterization techniques of polymer aging: from beginning to end, *Chem. Rev.* 123 (2023) 3007–3088, <https://doi.org/10.1021/acs.chemrev.2c00750>.
- [3] K. Adamsons, Predicting Service Life Performance: Our Analytical Toolbox, in: New developments in coatings technology, American Chemical Society, 2007, pp. 279–296, <https://doi.org/10.1021/bk-2007-0962.ch018>.
- [4] V. Baukh, H.P. Huinink, O.C.G. Adan, S.J.F. Erich, L.G.J. van der Ven, Predicting water transport in multilayer coatings, *Polymer* 53 (2012) 3304–3312, <https://doi.org/10.1016/j.polymer.2012.05.043>.
- [5] J.L. Gerlock, C.A. Smith, E.M. Núñez, V.A. Cooper, P. Liscombe, D.R. Cummings, T. G. Dusibiber, Measurements of Chemical Change Rates to Select Superior Automotive Clearcoats, in: Polymer durability, American Chemical Society, 1996, pp. 335–347, <https://doi.org/10.1021/ba-1996-0249.ch022>.
- [6] G. Almeida, S. Domenek, P. Perré, TransPoly: a theoretical model to quantify the dynamics of water transfer through nanostructured polymer films, *Polymer* 191 (2020) 122256, <https://doi.org/10.1016/j.polymer.2020.122256>.
- [7] L. Liu, S.E. Kentish, Modeling of carbon dioxide and water sorption in glassy polymers through PC-SAFT and NET PC-SAFT, *Polymer* 104 (2016) 149–155, <https://doi.org/10.1016/j.polymer.2016.10.002>.
- [8] E.M. Davis, Y.A. Elabd, Water clustering in glassy polymers, *J. Phys. Chem. B* 117 (2013) 10629–10640, <https://doi.org/10.1021/jp405388d>.
- [9] D.M. Kroll, S.G. Croll, Heterogeneity in crosslinked polymer networks: Molecular dynamics simulations, in: M. Wen, K. Dušek (Eds.), Protective Coatings, Springer International Publishing, Cham, 2017, pp. 39–65, https://doi.org/10.1007/978-3-319-51627-1_2.
- [10] Y. Liu, Y. Lin, Y. Zhang, B. Cao, K. Wu, L. Wang, Understanding water diffusion behaviors in epoxy resin through molecular simulations and experiments, *Langmuir* 40 (2024) 4871–4880, <https://doi.org/10.1021/acs.langmuir.3c03766>.
- [11] V. Baukh, H.P. Huinink, O.C.G. Adan, S.J.F. Erich, L.G.J. van der Ven, Water-Polymer Interaction during Water Uptake, *Macromolecules* 44 (2011) 4863–4871, <https://doi.org/10.1021/ma102889u>.
- [12] P. Gilormini, J. Verdu, On the role of hydrogen bonding on water absorption in polymers, *Polymer* 142 (2018) 164–169, <https://doi.org/10.1016/j.polymer.2018.03.033>.
- [13] J. Shen, X. Lin, J. Liu, X. Li, Effects of cross-link density and distribution on static and dynamic properties of chemically cross-linked polymers, *Macromolecules* 52 (2019) 121–134, <https://doi.org/10.1021/acs.macromol.8b01389>.
- [14] P.T.M. Albers, L.G.J. van der Ven, R.A.T.M. van Benthem, A.C.C. Esteves, G. de With, Water swelling behavior of poly(ethylene glycol)-based polyurethane networks, *Macromolecules* 53 (2020) 862–874, <https://doi.org/10.1021/acs.macromol.9b02275>.
- [15] C. Li, A. Strachan, Molecular scale simulations on thermoset polymers: a review, *J. Polym. Sci. B Polym. Phys.* 53 (2015) 103–122, <https://doi.org/10.1002/polb.23489>.
- [16] T.E. Gartner, A. Jayaraman, Modeling and simulations of polymers: a roadmap, *Macromolecules* 52 (2019) 755–786, <https://doi.org/10.1021/acs.macromol.8b01836>.
- [17] A. Iscen, N.C. Forero-Martinez, O. Valsson, K. Kremer, Acrylic paints: an atomistic view of polymer structure and effects of environmental pollutants, *J. Phys. Chem. B* 125 (2021) 10854–10865, <https://doi.org/10.1021/acs.jpcb.1c05188>.
- [18] E. Lin, X. You, R.M. Kriegel, R.D. Moffitt, R.C. Batra, Atomistic to coarse grained simulations of diffusion of small molecules into polymeric matrix, *Comput. Mater. Sci.* 138 (2017) 448–461, <https://doi.org/10.1016/j.commatsci.2017.07.011>.
- [19] Z. Li, F. Yuan, K.A. Fitchhorn, S.T. Milner, R.G. Larson, Molecular view of polymer/water interfaces in latex paint, *Macromolecules* 47 (2014) 6441–6452, <https://doi.org/10.1021/ma500866f>.
- [20] F. Vuković, T.R. Walsh, Moisture ingress at the molecular scale in hydrothermal aging of fiber–epoxy interfaces, *ACS Appl. Mater. Interfaces* 12 (2020) 55278–55289, <https://doi.org/10.1021/acsami.0c17027>.
- [21] A. Wang, C. Breakwell, F. Foglia, R. Tan, L. Lovell, X. Wei, T. Wong, N. Meng, H. Li, A. Seel, M. Sarter, K. Smith, A. Alvarez-Fernandez, M. Furedi, S. Guldin, M. M. Britton, N.B. McKeown, K.E. Jelfs, Q. Song, Selective ion transport through hydrated micropores in polymer membranes, *Nature* 635 (2024) 353–358, <https://doi.org/10.1038/s41586-024-08140-2>.
- [22] A. de Nicola, A. Correa, G. Milano, P. La Manna, P. Musto, G. Mensitieri, G. Scherillo, Local structure and dynamics of water absorbed in poly(ether imide): a hydrogen bonding anatomy, *J. Phys. Chem. B* 121 (2017) 3162–3176, <https://doi.org/10.1021/acs.jpcb.7b00992>.
- [23] S. Mani, F. Khabaz, R.V. Godbole, R.C. Hedden, R. Khare, Structure and hydrogen bonding of water in Polyacrylate gels: effects of polymer hydrophilicity and water concentration, *J. Phys. Chem. B* 119 (2015) 15381–15393, <https://doi.org/10.1021/acs.jpcb.5b08700>.
- [24] F. Khabaz, S. Mani, R. Khare, Molecular origins of dynamic coupling between water and hydrated Polyacrylate gels, *Macromolecules* 49 (2016) 7551–7562, <https://doi.org/10.1021/acs.macromol.6b00938>.
- [25] D. Aryal, M.P. Howard, R. Samanta, S. Antoine, R. Segelman, T.M. Truskett, V. Ganeshan, Influence of pore morphology on the diffusion of water in triblock copolymer membranes, *J. Chem. Phys.* 152 (2020) 1–9, <https://doi.org/10.1063/1.5128119>.
- [26] A.T. Kuo, W. Shinoda, S. Okazaki, Molecular dynamics study of the morphology of hydrated perfluorosulfonic acid polymer membranes, *J. Phys. Chem. C* 120 (2016) 25832–25842, <https://doi.org/10.1021/acs.jpcc.6b08015>.
- [27] F. Foglia, Q. Berrod, A.J. Clancy, K. Smith, G. Gebel, V.G. Sakai, M. Appel, J.-M. Zanotti, M. Tyagi, N. Mahmoudi, T.S. Miller, J.R. Varcoe, A.P. Periasamy, D.J. L. Brett, P.R. Shearing, S. Lyonnard, P.F. McMillan, Disentangling water, ion and polymer dynamics in an anion exchange membrane, *Nat. Mater.* 21 (2022) 555–563, <https://doi.org/10.1038/s41563-022-01197-2>.
- [28] S. Li, X. Zhang, J. Su, Desalination performance in Janus graphene oxide channels: geometric asymmetry vs charge polarity, *ACS Appl. Mater. Interfaces* 16 (2024) 2659–2671, <https://doi.org/10.1021/acsami.3c16592>.
- [29] S. Li, X. Zhang, J. Su, Enhanced rectification performance in bipolar Janus graphene oxide channels by lateral electric fields, *Langmuir* 40 (2024) 5488–5498, <https://doi.org/10.1021/acs.langmuir.4c00021>.
- [30] R.D. Guha, O. Idolor, L. Grace, An atomistic simulation study investigating the effect of varying network structure and polarity in a moisture contaminated epoxy network, *Comput. Mater. Sci.* 179 (2020) 109683, <https://doi.org/10.1016/j.commatsci.2020.109683>.
- [31] J. Shen, Y. Cai, C. Zhang, W. Wei, C. Chen, L. Liu, K. Yang, Y. Ma, Y. Wang, C.-C. Tseng, J.-H. Fu, X. Dong, J. Li, X.-X. Zhang, L.-J. Li, J. Jiang, I. Pinna, V. Tung, Y. Han, Fast water transport and molecular sieving through ultrathin ordered conjugated-polymer-framework membranes, *Nat. Mater.* 21 (2022) 1183–1190, <https://doi.org/10.1038/s41563-022-01325-y>.
- [32] L. De Keer, K.I. Kilic, P.H.M. Van Steenberge, L. Daelemans, D. Kodura, H. Frisch, K. De Clerck, M.-F. Reyniers, C. Barner-Kowollik, R.H. Dauskardt, D.R. D’hooge, Computational prediction of the molecular configuration of three-dimensional network polymers, *Nat. Mater.* 20 (2021) 1422–1430, <https://doi.org/10.1038/s41563-021-01040-0>.
- [33] K.B. Daly, J.B. Benziger, A.Z. Panagiotopoulos, P.G. Debenedetti, Molecular dynamics simulations of water permeation across nafion membrane interfaces, *J. Phys. Chem. B* 118 (2014) 8798–8807, <https://doi.org/10.1021/jp5024718>.
- [34] A. Kusoglu, A.Z. Weber, Water transport and sorption in nafion membrane, *ACS Symp. Ser.* 1096 (2012) 175–199, <https://doi.org/10.1021/bk-2012-1096.ch011>.
- [35] E.M. Davis, C.M. Stafford, K.A. Page, Elucidating water transport mechanisms in nafion thin films, *ACS Macro Lett.* 3 (2014) 1029–1035, <https://doi.org/10.1021/mz500515b>.
- [36] A.T. Kuo, S. Urata, R. Koguchi, T. Sonoda, S. Kobayashi, M. Tanaka, Molecular dynamics study on the water mobility and side-chain flexibility of hydrated poly(ω -methoxyalkyl acrylate)s, *ACS Biomater. Sci. Eng.* 6 (2020) 6690–6700, <https://doi.org/10.1021/acsbiomaterials.0c01220>.
- [37] A.T. Kuo, T. Sonoda, S. Urata, R. Koguchi, S. Kobayashi, M. Tanaka, Elucidating the feature of intermediate water in hydrated poly(ω -methoxyalkyl acrylate)s by molecular dynamics simulation and differential scanning calorimetry measurement, *ACS Biomater. Sci. Eng.* 6 (2020) 3915–3924, <https://doi.org/10.1021/acsbiomaterials.0c00746>.
- [38] A.T. Kuo, S. Urata, R. Koguchi, T. Sonoda, S. Kobayashi, M. Tanaka, Effects of side-chain spacing and length on hydration states of poly(ω -methoxyethyl acrylate) analogues: a molecular dynamics study, *ACS Biomater. Sci. Eng.* 7 (2021) 2383–2391, <https://doi.org/10.1021/acsbiomaterials.1c00388>.
- [39] C. Wu, W. Xu, Atomistic simulation study of absorbed water influence on structure and properties of crosslinked epoxy resin, *Polymer* 48 (2007) 5440–5448, <https://doi.org/10.1016/j.polymer.2007.06.038>.
- [40] W. Li, L. Zhang, M. Zhang, S. Chen, Structures of graphene-reinforced epoxy coatings and the dynamic diffusion of guest water: a molecular dynamics study, *Ind. Eng. Chem. Res.* 59 (2020) 20749–20756, <https://doi.org/10.1021/acs.iecr.0c04673>.
- [41] S. Pandiyan, J. Krajniak, G. Samaey, D. Roose, E. Nies, A molecular dynamics study of water transport inside an epoxy polymer matrix, *Comput. Mater. Sci.* 106 (2015) 29–37, <https://doi.org/10.1016/j.commatsci.2015.04.032>.
- [42] D. Xin, Q. Han, Investigation of moisture diffusion in cross-linked epoxy moulding compound by molecular dynamics simulation, *Mol. Simul.* 39 (2013) 322–329, <https://doi.org/10.1080/08927022.2012.725204>.

- [43] S. Morsch, S. Lyon, P. Greensmith, S.D. Smith, S.R. Gibbon, Water transport in an epoxy-phenolic coating, *Prog. Org. Coat.* 78 (2015) 293–299, <https://doi.org/10.1016/j.porgcoat.2014.08.006>.
- [44] R.D. Guha, O. Idolor, K. Berkowitz, M. Pasquinelli, L.R. Grace, Exploring secondary interactions and the role of temperature in moisture-contaminated polymer networks through molecular simulations, *Soft Matter* 17 (2021) 2942–2956, <https://doi.org/10.1039/d0sm02009e>.
- [45] S.M. Mousavifard, H. Ghermezcheshme, A. Mirzaalipour, M. Mohseni, G. de With, H. Makki, PolySMart: a general coarse-grained molecular dynamics polymerization scheme, *Mater. Horiz.* 10 (2023) 2281–2296, <https://doi.org/10.1039/d3mh00088e>.
- [46] W.L. Jorgensen, J. Tirado-Rives, The OPLS [optimized potentials for liquid simulations] potential functions for proteins, energy minimizations for crystals of cyclic peptides and crambin, *J. Am. Chem. Soc.* 110 (1988) 1657–1666, <https://doi.org/10.1021/ja00214a001>.
- [47] J.L.F. Abascal, C. Vega, A general purpose model for the condensed phases of water: TIP4P/2005, *J. Chem. Phys.* 123 (2005) 234505, <https://doi.org/10.1063/1.2121687>.
- [48] B. Hess, H. Bekker, H.J.C. Berendsen, J.G.E.M. Fraaije, LINCS: a linear constraint solver for molecular simulations, *J. Comput. Chem.* 18 (1997) 1463–1472, [https://doi.org/10.1002/\(SICI\)1096-987X\(199709\)18:12<1463::AID-JCC4>3.0.CO;2-H](https://doi.org/10.1002/(SICI)1096-987X(199709)18:12<1463::AID-JCC4>3.0.CO;2-H).
- [49] P. Bauer, B. Hess, E. Lindahl, GROMACS 2022 6 Source code, 2023, <https://doi.org/10.5281/zenodo.8134375>.
- [50] P.C.T. Souza, R. Alessandri, J. Barnoud, S. Thallmair, I. Faustino, F. Grünewald, I. Patmanidis, H. Abdizadeh, B.M.H. Bruijninks, T.A. Wassenaar, P.C. Kroon, J. Melcr, V. Nieto, V. Corradi, H.M. Khan, J. Domański, M. Javanainen, H. Martinez-Seara, N. Reuter, R.B. Best, I. Vattulainen, L. Monticelli, X. Periole, D. P. Tieleman, A.H. de Vries, S.J. Marrink, Martini 3: a general purpose force field for coarse-grained molecular dynamics, *Nat. Methods* 18 (2021) 382–388, <https://doi.org/10.1038/s41592-021-01098-3>.
- [51] G. Bussi, D. Donadio, M. Parrinello, Canonical sampling through velocity rescaling, *J. Chem. Phys.* 126 (2007) 14101, <https://doi.org/10.1063/1.2408420>.
- [52] M. Bernetti, G. Bussi, Pressure control using stochastic cell rescaling, *J. Chem. Phys.* 153 (2020) 114107, <https://doi.org/10.1063/5.0020514>.
- [53] D.R. Bauer, R.A. Dickie, Crosslinking chemistry and network structure in organic coatings - 2. Effect of catalysts on cure of melamine formaldehyde/acrylic copolymer films, *J. Polym. Sci. Part A-2, Polym. Phys.* 18 (1980) 2015–2025.
- [54] T.A. Wassenaar, K. Pluhackova, R.A. Böckmann, S.J. Marrink, D.P. Tieleman, Going backward: a flexible geometric approach to reverse transformation from coarse grained to atomistic models, *J. Chem. Theory Comput.* 10 (2014) 676–690, <https://doi.org/10.1021/ct400617g>.
- [55] L. Sarkisov, R. Bueno-Perez, M. Sutharson, D. Fairen-Jimenez, Materials informatics with PoreBlazer v4.0 and the CSD MOF database, *Chem. Mater.* 32 (2020) 9849–9867, <https://doi.org/10.1021/acs.chemmater.0c03575>.
- [56] M. Zhang, S.M. June, T.E. Long, Principles of step-growth polymerization (polycondensation and polyaddition) 5, 2012, pp. 7–47. BT-Polymer Science, <https://doi.org/10.1016/B978-0-444-53349-4.00131-X>.
- [57] I.K. McDonald, J.M. Thornton, Satisfying hydrogen bonding potential in proteins, *J. Mol. Biol.* 238 (1994) 777–793, <https://doi.org/10.1006/jmbi.1994.1334>.
- [58] A. Chandra, Effects of ion atmosphere on hydrogen-bond dynamics in aqueous electrolyte solutions, *Phys. Rev. Lett.* 85 (2000) 768–771, <https://doi.org/10.1103/PhysRevLett.85.768>.
- [59] D. Zhang, K. Li, Y. Li, H. Sun, J. Cheng, J. Zhang, Characteristics of water absorption in amine-cured epoxy networks: a molecular simulation and experimental study, *Soft Matter* 14 (2018) 8740–8749, <https://doi.org/10.1039/C8SM01516C>.
- [60] T. Greunz, C. Lowe, E. Bradt, S. Hild, B. Strauß, D. Stifter, A study on the depth distribution of melamine in polyester-melamine clear coats, *Prog. Org. Coat.* 115 (2018) 130–137, <https://doi.org/10.1016/j.porgcoat.2017.11.014>.
- [61] K. Adamsons, Chemical Depth Profiling of Automotive Coating Systems Using IR, UV-VIS, and HPLC Methods, in: Service life prediction, American Chemical Society, 2001, pp. 185–211, <https://doi.org/10.1021/bk-2002-0805.ch010>.
- [62] M. Rezayani, F. Sharif, H. Makki, Understanding ion diffusion in anion exchange membranes: effects of morphology and mobility of pendant cationic groups, *J Mater Chem A Mater* 10 (2022) 18295–18307, <https://doi.org/10.1039/d2ta04400e>.
- [63] R. Naohara, S. Namai, J. Kamiyama, T. Ikeda-Fukazawa, Structure and diffusive properties of water in polymer hydrogels, *J. Phys. Chem. B* 126 (2022) 7992–7998, <https://doi.org/10.1021/acs.jpcb.2c03069>.